

# Particle- $\gamma$ coincidences and coplanarity in the $^{32}\text{S} + ^{24}\text{Mg}$ binary reaction

C. Wheldon<sup>a,b,1</sup>, Tz. Kokalova<sup>a</sup>, W. von Oertzen<sup>a,c</sup>,  
B. Gebauer<sup>a</sup>, H.G. Bohlen<sup>a</sup>, Ch. Schulz<sup>a</sup>, S. Thummerer<sup>a</sup>,  
G. Efimov<sup>d</sup>, C. Beck<sup>e</sup>, D. Curien<sup>e</sup> and P. Papka<sup>e,2</sup>

<sup>a</sup>*SF7, Hahn-Meitner-Institut, Glienicker Straße 100, D-14109 Berlin, Germany.*

<sup>b</sup>*School of Physics and Astronomy, University of Birmingham, Edgbaston,  
B15 2TT, Birmingham, UK.*

<sup>c</sup>*Fachbereich Physik, Freie Universität Berlin, Arnimallee 14, D-14195 Berlin,  
Germany.*

<sup>d</sup>*Flerov Laboratory for Nuclear Reactions, Joint Institute for Nuclear Research,  
141980 Dubna, Moscow region, Russian Federation.*

<sup>e</sup>*Institut Pluridisciplinaire Hubert Curien – Département de Recherches  
Subatomiques, UMR7178, IN2P3-CNRS et Université Louis Pasteur  
(Strasbourg I), 23 Rue du Loess, B.P. 28, F-67037 Strasbourg Cedex 2, France.*

---

## Abstract

The reaction  $^{32}\text{S}$  (165.4 MeV) +  $^{24}\text{Mg}$  is studied using the binary reaction spectrometer (BRS) coupled to the EUROBALL germanium array. Particle-particle- $\gamma$  and particle- $\gamma$ - $\gamma$  coincidences have been examined. The  $Z$ -identification, position and energy information for binary reaction products are shown together with the Doppler-shift corrected  $\gamma$ -rays emitted from the fragments. Recent reports of evidence for hyper-deformation from angular correlations in similar data are also investigated. Analogous out-of-plane angular correlations are observed but attributed to reactions with the target contaminants  $^{16}\text{O}$  and  $^{12}\text{C}$ .

PACS numbers: 23.20.Lv (Gamma transitions and level energies), 25.70.Hi (Transfer reactions).

*Key words:* NUCLEAR REACTIONS  $^{24}\text{Mg} + ^{32}\text{S}$ ,  $E = 165.4$  MeV; measured particle- $\gamma$  coincidences, Doppler-shift correction, binary reactions, out-of-plane angular correlations, ternary fission  $Q_0$ -values.

## 1 Introduction

In-beam  $\gamma$ -ray spectroscopy has been dominated by the use of fusion-evaporation reactions populating a few nuclei to high angular momentum and with relatively large cross-sections. To reach the shortest-lived states, thin targets are used and the  $\gamma$ -rays emitted from the recoiling product nuclei are corrected for the Doppler shift, assuming a particular forward momentum. In contrast, binary reactions, utilising the same beam and target nuclei, can access different regions of the  $N - Z$  plane and different excitation-energy regimes. However, the cross-sections for these reactions are generally smaller and due to the type of states populated (low-spin states) the  $\gamma$ -ray yield is dramatically lower, falling off sharply with multiplicity. Furthermore, the products are spread over a much larger proportion of the available solid angle (the products from fusion-evaporation reactions continue in the forward, approximately  $0^\circ$ , direction) and can have much larger recoil velocities compared with those of fusion-evaporation reactions, making a precise Doppler-shift correction of the subsequently emitted  $\gamma$  rays more difficult. The advent of radioactive beams providing exotic ions has also brought about a renaissance in the use of binary/transfer reactions (see *e.g.* Refs. [1–4]) since transferring a small number of nucleons to/from an already exotic ion can create otherwise hard-to-reach species. To successfully exploit such reactions it is necessary to precisely identify the angles and energies of the recoiling products and also to identify the products themselves with good efficiency. Here, we present results from an experiment using the Berlin Binary Reaction Spectrometer (BRS) coupled to the EUROBALL germanium array. Particle- $\gamma$  coincidences are measured for binary reactions, completely suppressing the fusion-evaporation events. The yields are discussed and compared to recent, related work [5,6], that claim evidence for hyper-deformed shapes in  $^{60}\text{Zn}$ . An independent analysis/interpretation of the present data (particle information only), similar to that for the  $^{60}\text{Zn}$  data, is to appear as Ref. [7].

## 2 Experimental method

An experiment was performed in April 2003 at the VIVITRON Tandem facility of the IReS at Strasbourg. A 165.4 MeV beam of 2–3 pA,  $^{32}\text{S}$  ions was used to bombard a  $2 \times 120 \mu\text{g cm}^{-2}$   $^{24}\text{Mg}$  target each foil being backed with  $10 \mu\text{g cm}^{-2}$  carbon. The target was located at the centre of the EUROBALL IV germanium detector array. In this case the array comprised 209 Ge-crystals: 15 cluster

---

<sup>1</sup> Corresponding author. E-mail: c.wheldon@bham.ac.uk,  
URL: <http://www.hmi.de/people/wheldon/>

<sup>2</sup> Present address: iThemba Labs, PO Box 722, Somerset West 7129, South Africa.

detectors at backward angles, each comprising 7 Ge crystals in one Compton suppression shield, and 25 clover detectors close to  $90^\circ$ , each comprising 4 Ge crystals within one suppression shield. The forward-angle tapered germanium detectors of EUROBALL were replaced by the two-arm BRS detector. This set-up [8,9] is shown in Fig. 1. Three trigger conditions were set, requiring:

- (i)  $\geq 2$ -Ge detectors to fire;
- (ii)  $\geq 1$  BRS detector; or
- (iii)  $\geq 1$  BRS and  $\geq 1$  Ge detector.

Typical rates for the three triggers were: (i) 11 kHz (94%); (ii) 500 Hz (4.3%); and (iii) 200 Hz (1.7%). For both the BRS-gated and EUROBALL-only data, the Ge multiplicities peak at one, but for the EUROBALL-only data multiplicities two and three are relatively much larger than for the BRS events. Radioactive sources of  $^{152}\text{Eu}$ ,  $^{133}\text{Ba}$  and  $^{56}\text{Co}$  at the target position were used to obtain energy and efficiency calibrations for the germanium detectors. Note that the last calibration point for the germanium crystals is therefore at 3.45 MeV. Beyond this, energies and efficiencies are extrapolated leading to increased uncertainties. However, the  $^{16}\text{O}$  peaks with published values of  $6128.63 \pm 0.04$  and  $6915.5 \pm 0.6$  keV are observed at  $6130 \pm 3$  and  $6920 \pm 6$  keV respectively, after performing the Doppler-shift correction. Similarly, the  $^{12}\text{C}$ ,  $4438.0 \pm 0.3$  keV energy [10] is measured here at  $4437 \pm 2$  keV. Due to the large number of germanium crystals, the calibration was automated using a custom written routine [CW] based on the RadWare [11] analysis package. Output from the RadWare peak-finding routines was used to systematically calculate linear calibration coefficients by checking all possible pairs of identified peaks against all possible pairs of known source energies. These coefficients were then used to test the match between the remaining peaks and source energies not used in the calculation of the coefficients. The ‘best fit’ coefficients were taken which matched the largest number of source peaks having the lowest  $\chi^2$ . A similar procedure is used for the online calibration at the RISING setup at GSI [12].

### 3 Overview of the BRS

Here, a few details of the BRS detector system are given. The BRS was designed and built in Berlin by B. Gebauer *et al.* [8,9]. The complete technical specification will appear as Ref. [13]. Some details can also be found in Refs. [14–17]. The first stage of each BRS detector comprises a low-pressure multi-wire chamber (MWC) providing the position ( $x$  and  $y$ ) information for the incoming ions. The second stage consists of a Bragg-curve ionisation chamber (BIC) delivering  $Z$  (*i.e.* element) identification and energy,  $E$ .

The telescopes have rectangular cross sections, widening conically from the

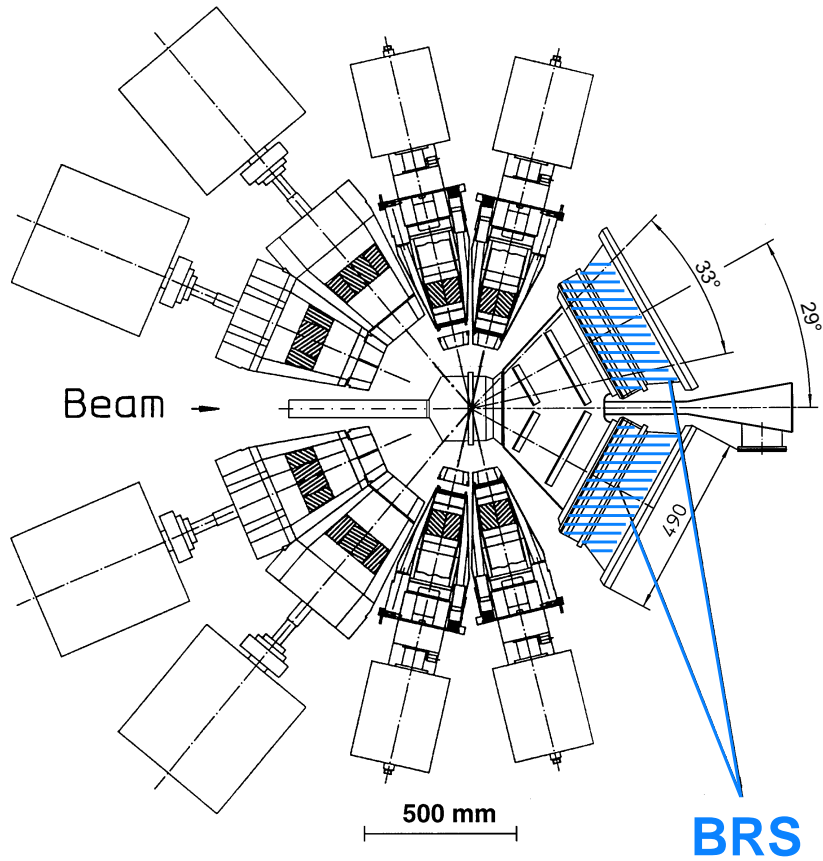


Fig. 1. Scale drawing showing the set-up of the BRS detectors at EUROBALL. The two BRS telescopes are stacked in a vertical configuration around the  $0^\circ$  beam axis. Close to  $90^\circ$  are the clover germanium detectors and at backward angles are the larger cluster germanium detectors.

MWCs to the BICs and the mounting at EUROBALL was such that the centre of the front plane of each telescope was 361.6 mm from the target position. This results in angular ranges for each telescope of:  $\theta=12.5^\circ \rightarrow 45.5^\circ$  and  $\phi=-16.5^\circ \rightarrow 16.5^\circ$ . In order to increase the count-rate capability, the resolution and the dynamic range, all detection planes of both detector stages are subdivided into four segments.

From each of the four BIC segments per telescope three signal types are derived:

(i) The Bragg-peak signal (*BP*), representing the maxima of the stopping (Bragg) curves of the reaction products in the counting gas and corresponding to the maximum amplitudes of the respective anode current pulses. The *BP* delivers *Z* information, unless the kinetic energy of the ions reaching the BIC is below the Bragg-maximum.

(ii) The range signal ( $R$ ), representing the range of ions in the active gas volume of the BIC, measured via the electron drift time, started with the quasi-prompt MWC timing signals and stopped with a timing signal derived from the anode at the back plane of the BIC, *i.e.* long ranges correspond to small  $R$  values (see Fig. 2).

(iii) The energy signal ( $E$ ), representing the kinetic energy of the ions after penetrating the MWC and the BIC entrance window, obtained by integrating the anode signal from the BIC.

### 3.1 Treatment of the BRS data

Below, the treatment of the BRS data in the offline analysis is described.

The BRS positions were calibrated using elastic scattering data collected with a  $210 \mu\text{g cm}^{-2}$   $^{197}\text{Au}$  target and using the known positions of slits in movable masks in front of the BRS telescopes (see Fig. 3). Events with good positions were used to define a BRS event as opposed to a EUROBALL-only event. From the position signals, the in-plane,  $\theta$ , and out-of-plane,  $\phi$ , angles are calculated. The BIC energy signals were calibrated using the end-point energies observed in the  $E$  versus  $BP$  plots (Fig. 4). The maximum kinetic energy deposited by the ions in the BIC was calculated using an energy-loss code, taking into account the window foils and gases. Following this procedure, the four segments could be summed together. (Note, that segment four of the first detector telescope could not be summed due to a different response profile and is treated separately in the subsequent analysis.) Following the gain-adjustment and summing of the BIC segment signals, they are matched to the position segments in case of multiple hits in the BICs caused by light charged particles, *i.e.* when two BIC segments fire, the segment used is that corresponding to the position signal. Next, a linear calibration was applied to the BIC signals on a run-by-run basis to correct for the accumulation of water vapour in the  $\text{CF}_4$  counting gas. This effect steadily decreased the amplitudes of these signals; an effect of 11% over the course of the experiment.

In addition to the above corrections, a series of gates have been applied to the data, the efficiencies of which are given in Table 1. This demonstrates that, of the events sorted, 94% are EUROBALL-only events as expected from the relative trigger rates in Section 2. BRS events with good position and BIC signals comprise  $\approx 1.3\%$  of the data whereas further demanding a  $\gamma$ -ray in coincidence with a ‘good’ BRS event reduces the data to  $\approx 0.2\%$ .

In addition to the above gates, events were also removed for which the total  $Z$  ( $Z_{tot.} = Z_1 + Z_2$ ) of the event was greater than the  $Z$  of the compound system, *i.e.*  $Z > 28$ . These were primarily events for which  $Z_{tot.}$  exceeded

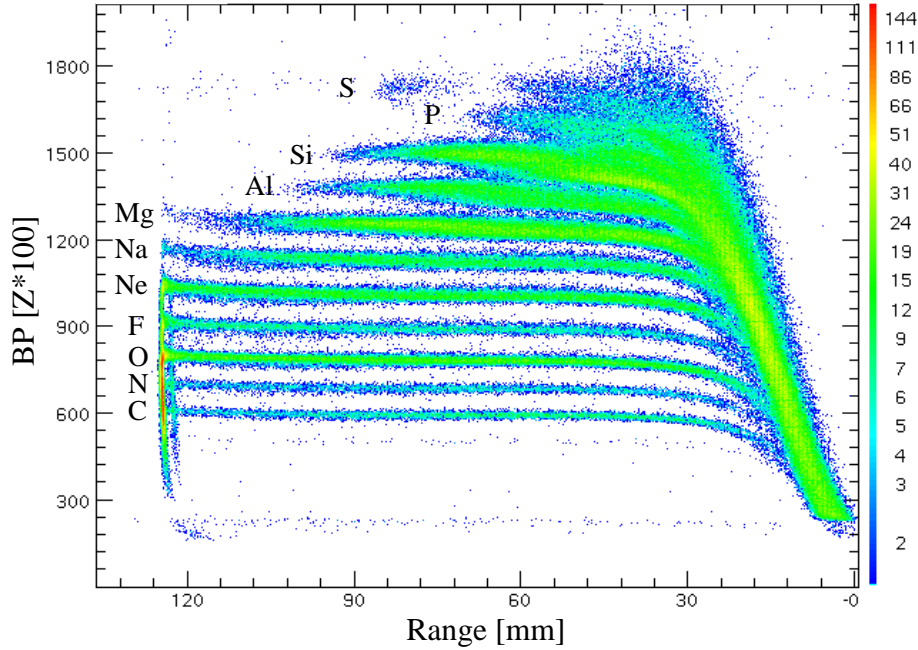


Fig. 2. A plot for telescope 2 showing range,  $R$  versus Bragg peak,  $BP$ . Each horizontal line corresponds to a different atomic charge,  $Z$  as labelled. The vertical axis is in units of  $\approx Z \times 100$ . The Bragg chamber is 125 mm deep. Relative intensity is shown on the side bar.

the  $Z$  of the compound system by 8 units, caused mainly by scattered beam particles entering the BRS telescopes in random coincidence.

### 3.2 Gamma-ray analysis

Following the processing of the BRS data, the  $\gamma$ -ray data could be processed as outlined below.

After the energy calibration and alignment of the germanium time signals an ‘addback’ routine was employed to recover the full  $\gamma$ -ray energies for instances where multiple germanium crystals in one detector fired. For the 7-crystal cluster detectors, the energy signals from up to three neighbouring crystals were added together. (Note: the middle crystal is considered as a neighbour to all other crystals in the surrounding ring.) Similarly for the 4-crystal clover detectors, all of the energy signals from up to (any) three crystals were added together. When adding signals together, the angles of each crystal that fired were averaged in preparation for the Doppler-shift correction. The above procedure increased the full-peak efficiency by a factor of  $\approx 1.4$  for energies above  $\sim 1$  MeV.

The Doppler-shift correction part of the analysis fell into two parts, both of

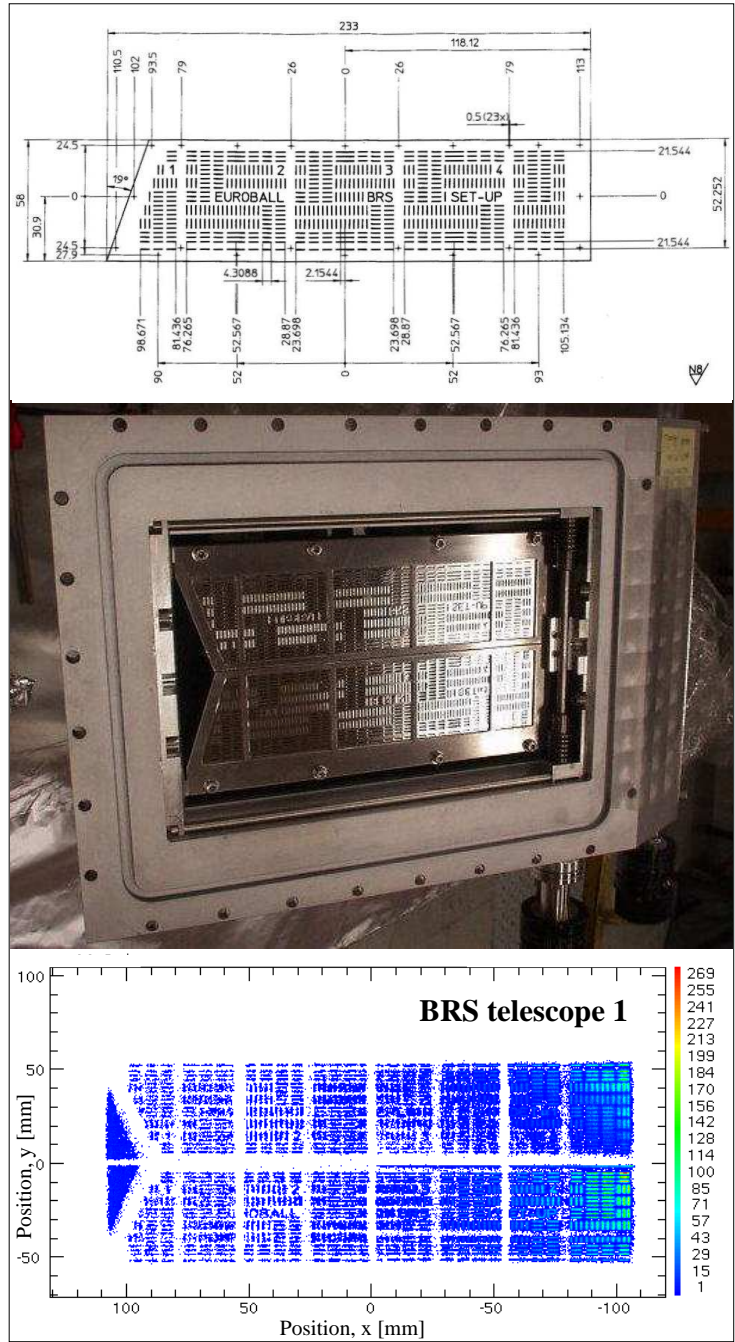


Fig. 3. (Top): technical drawing of one half of the BRS mask used for position calibration; (middle): photograph showing the two sides of the mask in place, in front of a BRS telescope; (bottom): calibrated position data ( $x$  versus  $y$  in mm) for telescope 1 using the  $^{197}\text{Au}$  target. The relative intensity ( $\propto$  counts) is shown on the side bar.

which use the following formula:

$$E_0 = E_{lab.} \left( \frac{1 - (v/c) \cdot \cos \theta}{\sqrt{1 - (v/c)^2}} \right) \quad (1)$$

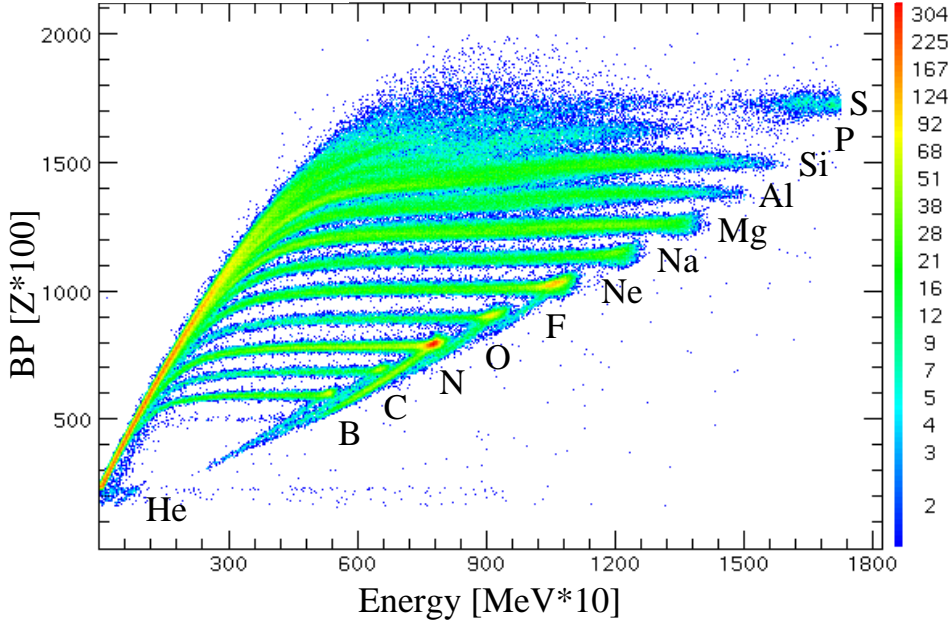


Fig. 4. A plot of energy,  $E$  versus Bragg peak,  $BP$  for BRS telescope 2. The horizontal scale is in  $\text{MeV} \times 10$  and the vertical scale  $\approx Z \times 100$ . The relative intensity ( $\propto$  counts) is shown on the side bar. The different elements (labelled) are well separated enabling unambiguous  $Z$  gates to be set. The end-point/punch-through energies for each element can be clearly seen.

where  $E_{lab.}$  and  $E_0$  are the observed and corrected  $\gamma$ -ray energies respectively,  $\theta$  is the angle between the recoiling nucleus and the Ge detector, and  $v$  is the recoil velocity. For those  $\gamma$ -events for which a BRS trigger was also recorded, the  $\gamma$  rays were Doppler-shift corrected using the angle information (provided by the BRS position and Ge-detector angle), the energy signal ( $E$ ) and  $Z$  gates. To calculate the velocity from the energy signal,  $N = Z$  was assumed for each element due to the absence of mass resolution in this measurement. (Note that the Doppler-shift correction for binary reactions (those without particle evaporation) could also be made using 2-body kinematics. The resulting FWHM for the  $\gamma$  rays is the same as from the method used here.) For those events containing no BRS trigger, only EUROBALL data, the events were Doppler-shift corrected by assuming an average forward velocity of  $v/c = 0.0615$ . This velocity was obtained iteratively by minimising the peak widths in the final spectrum. Furthermore, in each case, the non-Doppler corrected energies were also stored to provide a check for the Ge-energy alignment and calibration via the intense 511 keV,  $e^+e^-$  annihilation peak.

For the BRS-triggered  $\gamma$  rays the FWHM is 17.5 keV (0.99%) at 1.8 MeV, whereas for the EUROBALL-only data the value is  $\approx 23$  keV (1.3-1.4%) at 1.8 MeV.

After performing the above procedure using the graphical sorting-software DATA8M [18], the  $\gamma$  rays were written out to a series of RadWare-format [11]

Table 1

Gates and their efficiencies for a typical run:  $\approx 1.5\%$  of the total data. For each gate the percentage transmission is quoted. “EUROBALL-only” means events with no BRS; “BRS-Position” means  $x$  and  $y$  signal in the BRS; “Good pos.” means that the BRS positions lie within the segment limits; “Good  $BP$ ” means  $BP$  and  $E$  signals in the same segment as the position signals; “Good  $Z$ ”, means that the BIC signals were such as to lie within a  $Z$ -gate *i.e.* on the  $E$  versus  $BP$  plot the  $Z$  was unambiguous.

Gate/condition	Telescope 1		Telescope 2	
	No. of events (%)			
Events sorted: 34,472,372				
EUROBALL-only	32,506,040	(94%)	32,590,766	(94%)
BRS-Position	1,937,673	(5.6%)	1,832,596	(5.3%)
<i>Good Pos.</i>	622,565	(1.8%)	622,326	(1.8%)
Good $BP$	1,122,787	(3.2%)	1,195,897	(3.4%)
<i>Good Pos. &amp; BP</i>	426,619	(1.2%)	487,005	(1.4%)
<i>Good Pos. &amp; Z</i>	189,719	(0.6%)	326,832	(1.0%)
All events with $\gamma$ rays: 29,319,929 (85%)				
Good BRS- $\gamma$ events with multiplicity $>0$	47,096	(0.14%)	82,456	(0.24%)

histograms. Of these the following are of primary interest here:

- $\gamma\gamma\gamma$ : a 3-dimensional  $\gamma$ - $\gamma$ - $\gamma$  cube containing Doppler-shift corrected  $\gamma$  rays for which no BRS trigger was present.
- $brs$ - $\gamma\gamma$ : a 2-dimensional  $\gamma$ - $\gamma$  matrix containing all Doppler corrected  $\gamma$ -ray events with BRS triggers.
- $brs$ - $\gamma$ : 1-dimensional singles spectra for each BRS telescope containing all  $\gamma$  rays with a BRS trigger.

The results from this analysis are discussed in the following section.

## 4 Results

### 4.1 BRS triggered data

Plotting  $E$  versus  $BP$  for each BRS telescope enabled a series of  $Z$  gates to be set on the data to define the element for both the Doppler-shift correction and for separating the  $\gamma$  rays from different product species. Following this step, the  $\gamma$  rays for each product can be examined under various conditions. Examples of BRS- $\gamma$  coincidences are shown in Fig. 5. As can be seen, from the BRS- $\gamma$  projection (Fig. 5 (top)), the most prominent decays originate from deformed nuclei close to the target and/or beam nuclei. The most intense are  $^{24}\text{Mg}$  (target),  $^{20}\text{Ne}$  and  $^{28}\text{Si}$ . Indeed, one of the most intense  $\gamma$ -ray transitions observed in these data is the 1779 keV  $2^+ \rightarrow 0^+$  transition in  $^{28}\text{Si}$ , clearly seen in Fig. 5 (middle). The cleanliness of the  $Z$  separation is demonstrated by contrasting this Si-gated spectrum with that of the corresponding Al-gated spectrum (Fig. 5 (bottom)). No leak-through of the intense silicon lines is seen in the Al spectrum. Furthermore, the Al spectrum demonstrates the power of the BRS to select relatively weak channels from a large background of events. One interesting point to note is the 417 keV  $^{26}\text{Al}$ ,  $3^+ \rightarrow 5^+$   $\gamma$ -ray transition (the lowest in  $^{26}\text{Al}$ ) highlighted in Fig. 5 (bottom). The 417 keV level has a half-life of  $t_{1/2} = 1.25 \pm 0.03$  ns [19] and yet appears as a sharp line in Fig. 5 (bottom). This is because the recoil velocity at  $30^\circ$  is  $v/c \approx 0.09$ , implying a flight time from the target to the front of the BRS of  $\approx 13$  ns. Therefore, any states with lifetimes of the order of ten nanoseconds or less will decay in-view of the germanium detectors and be visible as sharp lines in the BRS gated spectra. Decays exceeding several tens of nanoseconds will not be observed.

The spectra shown in Fig. 5 are  $\gamma$ -ray singles spectra gated by particles in the BRS. However, there are sufficient statistics for particle- $\gamma$ - $\gamma$  coincidences. Figure 6 shows the total projection of the  $brs$ - $\gamma\gamma$  matrix and the spectrum gated by the 440 keV  $5/2^+ \rightarrow 3/2^+$  transition in  $^{23}\text{Na}$ . The decays, in  $^{23}\text{Na}$  are clearly visible up to the  $11/2^+$  state at 5534 keV. This channel is 1-proton lighter than the  $^{24}\text{Mg}$  target.

One further feature of the BRS data is the ability to define a binary reaction by setting two  $Z$  gates; one on each BRS telescope. This enables the precise definition of a reaction and is demonstrated in Section 5.

### 4.2 Euroball-only data

In Table 1 the events are broken down into the various triggers, 94% of which constitute EUROBALL-only (*i.e.*  $\gamma$ -only) data. The total projection of the  $\gamma\gamma$

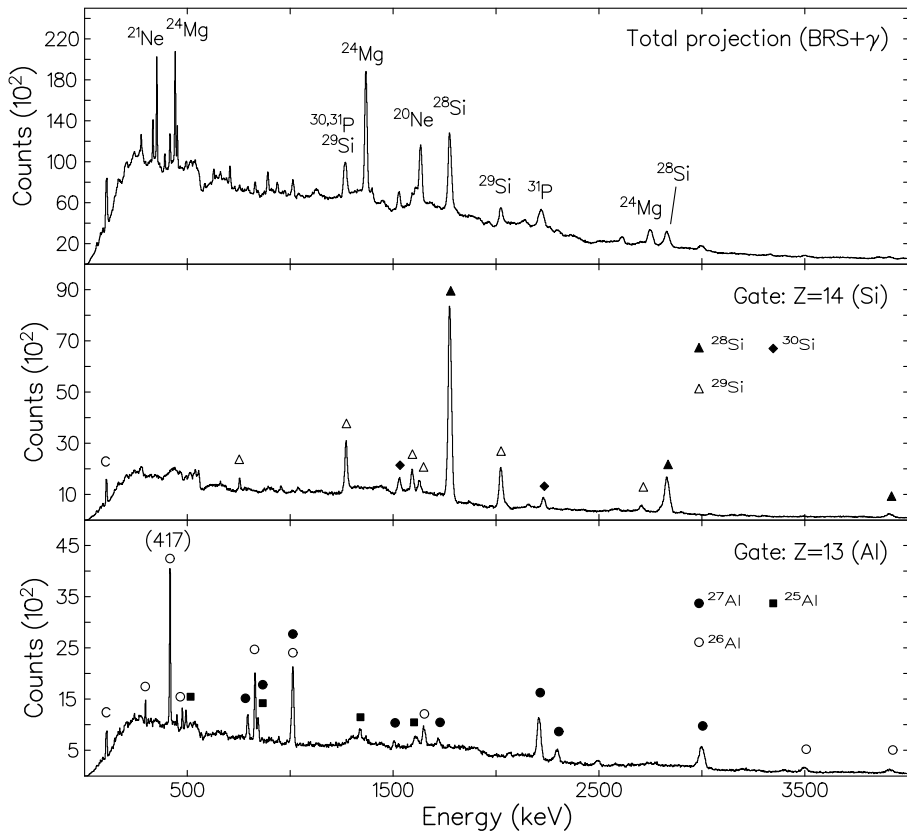


Fig. 5. BRS-gated spectra. (Top): full singles spectrum gated by BRS events with well-defined  $Z$ ; (middle): spectrum gated by  $Z = 14$  (silicon); (bottom):  $Z = 13$  (aluminium) gated spectrum. The isotope(s) contributing to the most prominent peaks are indicated. In the bottom spectrum the 417 keV peak energy is also quoted. See text for details. Both  $Z$ -gated spectra represent the sum from gating on each BRS telescope. A contaminant from neutron activation in the germanium detectors is labelled 'c'.

histogram is shown in Fig. 7 (top). Two of the most intense products are  $^{46}\text{Ti}$  and  $^{50}\text{Cr}$  isotopes corresponding to  $2\alpha 2p$  and the  $\alpha 2p$  evaporation channels respectively. Setting double gates on the  $\gamma$ -ray energies enables a very clean selection of a particular channel, the case for  $^{50}\text{Cr}$  is shown in Fig. 7 (bottom).

The distribution of isotopes identified in these data is shown in Fig. 8 and falls into three groups. The main population is from the  $^{32}\text{S} + ^{24}\text{Mg}$  reaction. The second, to the neutron-rich side of the vertical dashed line are products from reactions with aluminium in the target frame and are relatively weak. The third population starting with calcium and lighter isotopes is from oxygen and carbon (backing) in the  $^{24}\text{Mg}$  target. Examining the latter group of isotopes in more detail, it is apparent that the observed peaks lie systematically lower in energy than the literature values. *E.g.* for  $^{41}\text{K}$ , the 1677.2 keV transition [20] is observed at 1662 keV. This shift implies a Doppler correction using a higher velocity of  $v/c \approx 0.08$  is required (the germanium detectors lie at predominantly

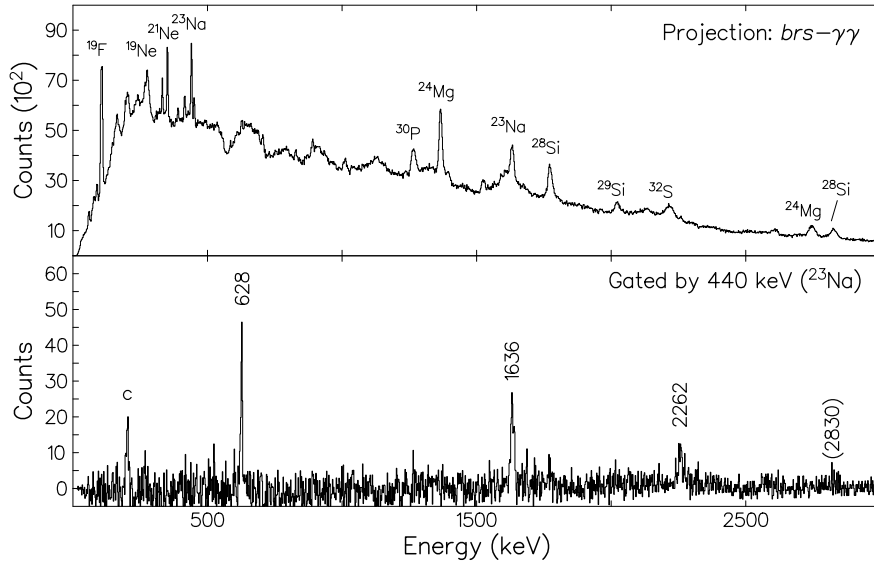


Fig. 6. BRS- $\gamma$ - $\gamma$  coincidence spectra. (Top): total projection of the *brs*- $\gamma$  $\gamma$  matrix; (bottom): background-subtracted spectrum gated by the 440 keV  $5/2^+ \rightarrow 3/2^+$  transition in  $^{23}\text{Na}$ . Transitions in  $^{23}\text{Na}$  are labelled with energies. A contaminant at 202 keV is labelled 'c'.

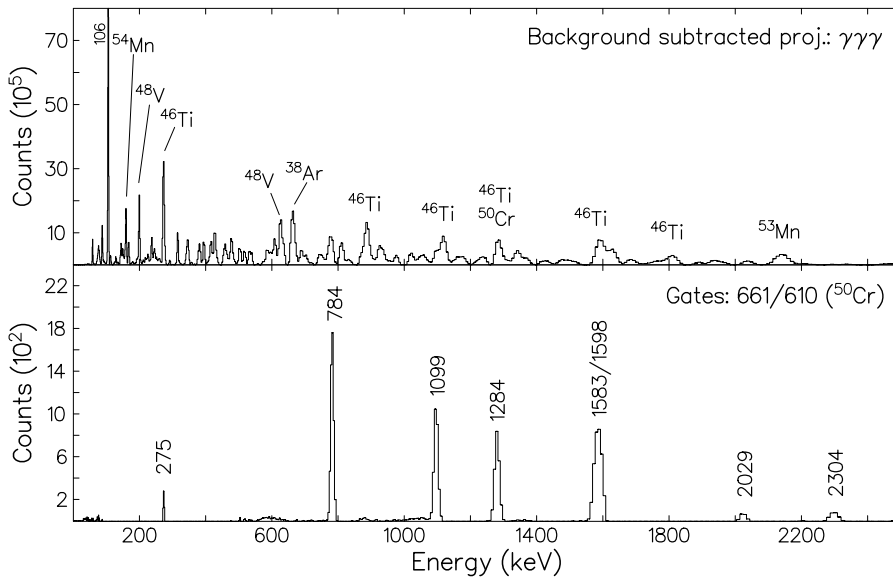


Fig. 7. Spectra from the EUROBALL-only data. (Top): background-subtracted total projection of the  $\gamma\gamma\gamma$  cube; (bottom): background-subtracted spectrum, double gated by the 661 and 610 keV transitions in  $^{50}\text{Cr}$ . Transitions up to the  $14^+$  state at 9917 keV can be identified. Note the different vertical scales.

backward angles; the average in-plane Ge angle is  $115.57^\circ$ ), consistent with fusion-evaporation reactions with a target  $\sim 10$  mass units lighter than  $^{24}\text{Mg}$ , half way between that for  $^{16}\text{O}$  (a shift of 8 mass units from  $^{24}\text{Mg}$ ) and  $^{12}\text{C}$  (a shift of 12 mass units). More details on this aspect of the data are given in the next section.

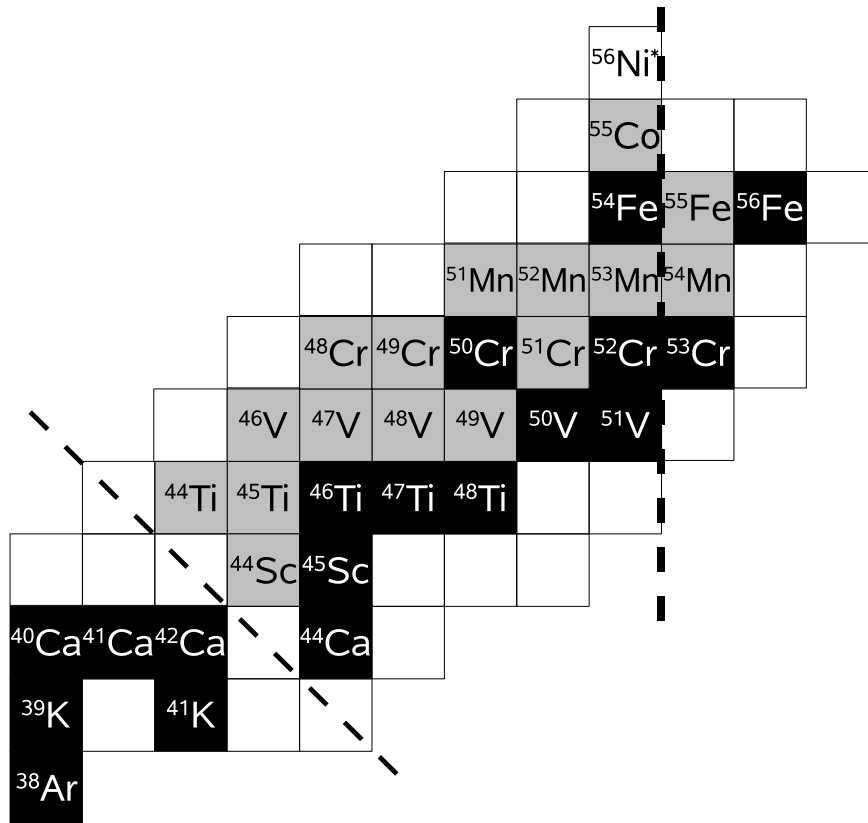


Fig. 8. Plot showing the isotopes observed in the EUROBALL-only data using a ‘classic’ Doppler correction ( $v/c = 0.0615$ ). All of the labelled isotopes have been identified with the exception of the compound nucleus,  $^{56}\text{Ni}^*$ , shown here only for orientation. Black squares indicate naturally abundant isotopes. See text for details.

## 5 Discussion

Recently, BRS data have been used to claim evidence for hyper-deformation in  $^{60}\text{Zn}$  [5,6]. There are many similarities between the  $^{60}\text{Zn}$  data and the present  $^{56}\text{Ni}$  data, including the use of the BRS coupled to a germanium detector array. Therefore, it is worthwhile considering the evidence for hyper-deformed nuclei in light of the new data.

Firstly, a summary of the analysis and interpretation presented in Refs. [5,6] is given below. In Ref. [5,6], the data were obtained with the BRS telescopes in coincidence with the OSIRIS  $\gamma$ -ray detector array [21]. The primary evidence in favour of hyper-deformed shapes was obtained from particle-particle coincidences following the reaction:  $^{24}\text{Mg}(^{36}\text{Ar}, ^{60}\text{Zn}^*)$  at  $E_{beam} = 195$  MeV. In particular, the out-of-plane correlations were examined by plotting  $\phi_{1-2}$  ( $=\phi_1 - \phi_2$ ). For binary reactions with no ‘missing’ charge, this is a sharp correlation distributed around  $180^\circ$  because the two products are coplanar. Where additional particles are emitted, for example an  $\alpha$ -particle ( $\Delta Z = -2$ ) or

proton ( $\Delta Z = -1$ ), this distribution becomes broad, as the two primary binary fragments are no longer coplanar. As more and more particles are emitted/evaporated it is expected that these out-of-plane correlations become broader and broader. However, in the  $^{60}\text{Zn}^*$  data this is not the case for all the distributions. In fact, examining successive channels with increasing ‘missing’ charge, the distributions are broad for the  $\Delta Z = -2$  case, then a sharp component above an increasingly broad background appears for the  $\Delta Z = -4$  and  $-6$  channels before returning to a purely broad distribution for all subsequent channels.

In Refs. [5,6], the authors attribute this phenomenon to elongated compound nuclear shapes (hyper-deformation), with multiple  $\alpha$ -particles forming in the neck before fission occurs. After fissioning the  $\alpha$ -particles continue, essentially at rest in the centre-of-mass frame. Thus, the coplanarity of the two primary (heavy) binary products is preserved. It has been argued that due to the very negative  $Q$ -values for such ternary reactions (the  $\Delta Z = -4$  and  $-6$  channels), these reactions are only able to compete with binary fission because of the very elongated shapes adopted by the compound nucleus ( $^{60}\text{Zn}^*$ ) with contributions from the rotational energy at large angular momentum ( $44\hbar$  [5,6]) and shell-corrections playing a role.

The first publication of these correlations [15] explained the distributions as either arising from pre-scission evaporations, such that the out-of-plane correlations of the remaining fissioning system are undisturbed, or from the amalgamation of multiple  $\alpha$ -particle clusters in the neck of the di-nuclear system occurring before fission takes place. The pre-scission evaporation is unlikely since the energy carried away by the  $\alpha$ -particles would be large, leaving insufficient energy for the subsequent fission process [22,23]. Also, if pre-scission were responsible, the  $\Delta Z = \text{odd}$  channels would also exhibit these out-of-plane correlations. The second process of strongly aligned angular momentum vectors is discounted in Refs. [5,6] because no sharp out-of-plane correlations are observed in the  $1\alpha$  channel. However, a sharp  $\Delta Z = 2$  peak ought to be present if the scenario in which one  $\alpha$  particle is emitted from the neck can compete as fission takes place, despite its lower deformation. Also, there is no a priori reason why only two or three  $\alpha$  particles should exhibit this structure assuming highly deformed shapes.

In addition to the three processes outlined above, a fourth opportunity for causing sharp out-of-plane correlations exists. In Refs. [5–7,15] and the present data  $^{24}\text{Mg}$  targets have been used which contain both oxygen and carbon (backing). Reactions on oxygen would simulate binary reactions in which  $\Delta Z = -4$  and carbon would simulate the  $\Delta Z = -6$  channels. Whilst such a mechanism has been discussed in Refs. [5–7] it was reported to be unable to produce sufficient yields in the relevant reaction channels. This conclusion was reached after a quantitative comparison of the fission yields on  $^{24}\text{Mg}$  and

then by assuming that these differential cross-sections will remain the same for reactions on an  $^{16}\text{O}$  target. This analysis was carried out for several reaction channels. From such an analysis the estimated oxygen contents of the magnesium targets are  $\approx 45\%$  in the  $^{56}\text{Ni}$  [7] data and  $\approx 15\%$  in the  $^{60}\text{Zn}$  experiment [5,6]. (*Aside:* the oxidation levels are different because for the  $^{60}\text{Zn}$  experiment the targets were transferred under vacuum from the target laboratory to the scattering chamber by means of a target-lock system [14]. The vacuum quality in the chamber was also high. Conversely for the  $^{56}\text{Ni}$  EUROBALL experiment, the targets were stored unprotected prior to mounting and the subsequent vacuum was also significantly worse.) However, the  $Q$ -values, thresholds and centre-of-mass energies are different for reactions on  $^{16}\text{O}$  and indeed for  $^{12}\text{C}$  too. An independent way of obtaining these yields would be to run the experiment using pure  $^{16}\text{O}$  and  $^{12}\text{C}$  targets, without  $^{24}\text{Mg}$ , as is routinely done in other charged-particle spectroscopy measurements. In light of the present data, this aspect of sharp out-of-plane correlations for the  $\Delta Z = -4$  and  $-6$  channels will be investigated.

The current data for  $^{56}\text{Ni}^*$  will now be discussed in terms of the coplanarity of the fragments. Figure 9 shows the out-of-plane distributions for the present data for all reaction channels, from true binary reactions with no ‘missing’ charge ( $\Delta Z = 0$ ), up to reactions with  $\Delta Z = -8$ . (The yields corresponding to Fig. 9 are given in Table 2.) The binary,  $\Delta Z = -4$  and  $-6$  channels all show sharp distributions peaked around  $180^\circ$ , set on a broader background. (This broad background, is interpreted here (as for the  $^{60}\text{Zn}$  data [5,6]) as originating from reactions on  $^{24}\text{Mg}$  with increasing numbers of particles emitted/evaporated.) In addition to the presence of a narrow component in the  $\phi_{1-2}$  distributions, the highest yields are also observed for the  $\Delta Z = -4$  and  $-6$  channels. Looking in more detail at the narrow distributions the yields of each element are extracted for the binary,  $\Delta Z = -2$ ,  $-4$  and  $-6$  channels and are shown in Table 3. The yields for the narrow component of the  $\Delta Z = -4$  and  $-6$  channels are obtained by gating on a  $\phi_{1-2}$  versus  $E_{tot.}$  plot using a rectangular gate from  $177^\circ \rightarrow 183^\circ$  and all energies above 95 MeV (see inset of Fig. 10). Side-by-side with the  $Z$  distributions in Table 3, are the  $Q_0$ -values. A strong dependence of yield on  $Q_0$ -value is expected for binary reactions, the more negative  $Q_0$ -values being strongly suppressed. Indeed this effect is seen from the extent of the binary channels. The  $Q_0$ -values for stripping reactions are generally more favourable than the corresponding pick-up reactions, leading to  $Z$  distributions skewed towards products lighter than sulphur. For example, for  $\alpha$ -pick-up,  $Q_0 = -2.67$  MeV in contrast to  $\alpha$ -stripping with  $Q_0 = +3.04$  MeV. For the narrow out-of-plane components, two sets of  $Q_0$ -values are given. The first assumes that the products result from reactions on the target contaminants ( $^{16}\text{O}$  and  $^{12}\text{C}$ ), the second assumes particle emission/evaporation and a  $^{24}\text{Mg}$  target. Both sets of  $Q_0$ -values are consistent with the odd-even scattering in the data, with highly negative  $Q_0$ -values for odd- $Z$  products. This is correlated with reduced yield in those channels. How-

ever, the highest yield channels, for example the Si+O ( $\Delta Z = -6$ ) and Si+Ne ( $\Delta Z = -4$ ), can be easily explained from target contaminants, having positive or small negative  $Q_0$ -values. In this scenario, these two channels correspond to  $\alpha$  transfer on carbon and oxygen targets respectively. However in terms of ternary reactions, the  $Q_0$ -values are highly negative;  $-21$  and  $-16$  MeV for the Si+O and Si+Ne channels respectively. Shell-correction energies [24] and rotational energies are each calculated to be  $\sim 5$  MeV for a hyper-deformed  $^{56}\text{Ni}^*$  nucleus and are insufficient to explain the large yields. Indeed the yields are quite different from the  $^{24}\text{Mg}(^{36}\text{Ar}, ^{60}\text{Zn}^*)$  reaction of Refs. [5,6] where the peak yield appears to occur for the  $\Delta Z = -2$  channel in contrast to the  $-6$  channel in the present work. Again, this is most likely due to the different oxidation levels in the targets, as outlined earlier.

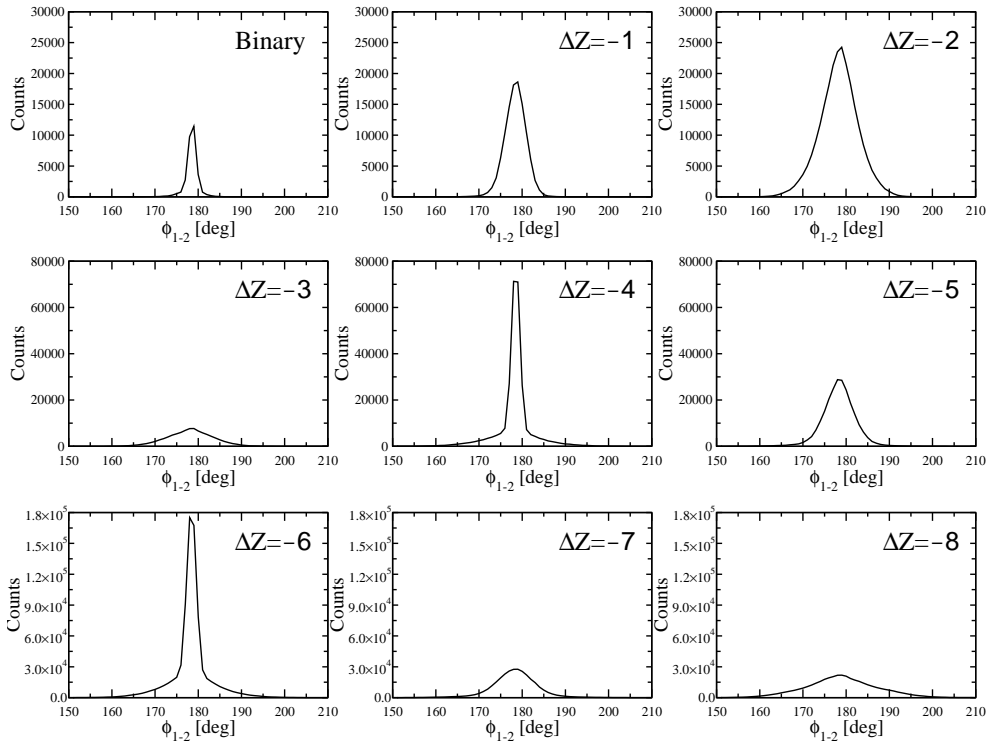


Fig. 9. Plot showing out-of-plane distributions,  $\phi_{1-2}$  for BRS coincidences gated by ‘missing’ charge,  $\Delta Z$ . Note the different vertical scales for each row. Sharp correlations are observed for the  $\Delta Z = -4$  and  $-6$  channels. A systematic error of  $-1.0^\circ$  is present in  $\phi_{1-2}$ .

Returning to the  $\gamma$ -ray data, spectra can be generated in coincidence with the narrow component of the out-of-plane correlation and  $Z = 9$  (F) and 15 (P) in the BRS telescopes. The resulting coincidences can be seen (Fig. 10). These represent the  $\Delta Z = -4$  channel and correspond to proton and deuteron transfer on an oxygen target. The spin distributions of binary partner events have also been examined to see if there is a different spin population for nuclei populated in reactions on the  $^{24}\text{Mg}$  target compared to the target contami-

Table 2

Yields (counts) as a function of  $\Delta Z$  for the out-of-plane distributions shown in Fig. 9. For the  $\Delta Z = -4$  and  $-6$  cases, the number of counts in the narrow component of the  $\phi_{1-2}$  distributions are also given.

$\Delta Z$	0	-1	-2	-3	-4	-5	-6	-7	-8
Yields (all)	31540	110301	239305	91788	271555	231357	784662	299676	389789
Yields (narrow)	—	—	—	—	206171	—	578056	—	—

Table 3

Distributions of binary reaction products by  $Z$ , assuming  $N = Z$  isotopes. Ground-state  $Q_0$ -values for each reaction are also quoted. For the  $\Delta Z = -4$  and  $-6$  reactions, two sets of  $Q_0$ -values (given in MeV) are quoted. The first assuming reactions on target contaminants ( $^{16}\text{O}$  and  $^{12}\text{C}$ ), the second assuming particle emission, *i.e.* ternary reactions. Only the narrow component of the  $\phi_{1-2}$  distributions are considered for  $\Delta Z = -4$  and  $-6$ . Products heavier than Cl could not be cleanly separated in this experiment.

$Z$	$Z$ distributions									
	Binary		$\Delta Z = -2$		$\Delta Z = -4$ (narrow)			$\Delta Z = -6$ (narrow)		
	Cnts	$Q_0$	Cnts	$Q_0$	Cnts	$Q_0^{16\text{O}}$	$Q_0^{\text{tern.}}$	Cnts	$Q_0^{12\text{C}}$	$Q_0^{\text{tern.}}$
5 (B)	—	—	—	—	—	—	—	53	-13.63	-34.83
6 (C)	—	—	—	—	—	—	—	69063	0.00	-21.21
7 (N)	—	—	—	—	279	-9.18	-23.22	54852	-8.68	-28.89
8 (O)	—	—	—	—	40380	0.00	-14.05	359155	+0.21	-20.99
9 (F)	—	—	97	-18.81	29411	-11.43	-25.47	25694	-14.68	-35.89
10 (Ne)	—	—	49359	-9.32	81777	-2.22	-16.26	61908	-5.04	-26.25
11 (Na)	20	-10.33	17890	-16.99	23751	-13.36	-27.41	14662	-15.65	-36.86
12 (Mg)	16165	0.00	157233	-6.95	61146	-2.89	-16.93	61908	-5.04	-26.25
13 (Al)	4205	-7.54	29452	-17.95	23751	-13.36	-27.41	25694	-14.68	-35.89
14 (Si)	22300	3.04	157233	-6.95	81777	-2.22	-16.26	359155	+0.21	-20.99
15 (P)	4205	-7.54	17890	-16.99	29411	-11.43	-25.47	54852	-8.68	-28.89
16 (S)	16165	0.00	49359	-9.32	40380	0.00	-14.05	69063	0.00	-21.21
17 (Cl)	20	-10.33	97	-18.81	279	-9.18	-23.22	53	-13.63	-34.83

nants. This was undertaken by plotting, for example for  $^{28}\text{Si}$ , the  $\gamma$ -ray yield ratio:  $\frac{I_\gamma(4_1^+ \rightarrow 2_1^+)}{I_\gamma(2_1^+ \rightarrow 0_1^+)}$  as a function of binary partner, *i.e.*  $Z$ . However, within the uncertainties a constant ratio was observed, the weighted mean of which is  $0.27 \pm 0.01$ . Similarly for transitions in  $^{29}\text{Si}$ , no significant change in spin pop-

ulation has been observed as the partner  $Z$  is varied. This is perhaps not surprising since the  $\gamma$  rays examined here are from relatively low-spin states and are therefore easily populated in both the  $^{32}\text{S} + ^{24}\text{Mg}$  reactions and the reactions on  $^{16}\text{O}$  and  $^{12}\text{C}$ .

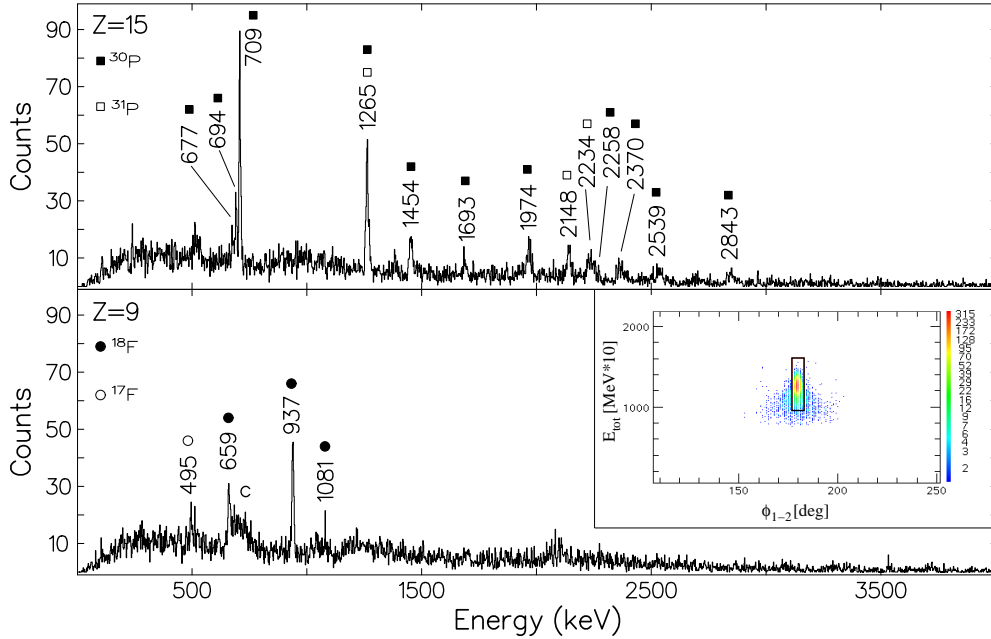


Fig. 10. Coincident  $\gamma$ -ray spectra generated by gating on  $Z = 9$  (fluorine, bottom) and 15 (phosphorus, top) in the BRS telescopes. Additionally a gate on the narrow component of the out-of-plane distribution is set (box in the inset) on the  $\phi_{1-2}$  versus  $E_{tot.}(= E_1 + E_2)$  matrix gated by  $Z_1 = 9$  and  $Z_2 = 15$ . A broad contaminant peak in the fluorine spectrum, indicated by ‘c’, arises from the strong coincident 709 keV transition in phosphorus being wrongly Doppler-shift corrected.

Finally, it is striking that the only sharp distributions after the binary reaction channel are those corresponding to target contaminants. Products from target contaminants lighter than magnesium have been observed in the EUROBALL-only data (Fig. 8); confirmed by the shift seen in the Doppler correction necessary to reproduce the published transition energies (Section 4.2). The small sharp peak in the out-of-plane correlation reported in Refs.[5,6] for the  $\Delta Z = -8$  channel is not seen here (see Fig. 9). Furthermore, this phenomenon has only been observed using  $^{24}\text{Mg}$  targets. It would be elucidating to perform experiments using a similar detector set-up but with different beam and target combinations to firmly tie down the mechanism responsible.

## 6 Summary

In summary, data taken in coincidence with the EUROBALL germanium detector array and the Binary Reaction Spectrometer have been presented. The

BRS was able to sensitively select binary reactions between a 165.4 MeV  $^{32}\text{S}$  beam and a  $^{24}\text{Mg}$  target representing only a small percentage of the total number of events. The treatment of the data has been outlined, and the quality of the Doppler-shift correction shown for events both with and without the BRS. Furthermore, the present data from the BRS have been used to examine the recent claims of hyper-deformation at high angular momentum. In contrast to the published BRS data showing tentative evidence for such an effect in  $^{60}\text{Zn}^*$ , the data here for  $^{56}\text{Ni}^*$  are interpreted as being compatible with target contaminants. Specifically, the out-of-plane angular correlations for coplanar reactions have been investigated for reactions with  $\Delta Z \geq 0$  and the narrow distributions for  $\Delta Z = -4$  and  $-6$  found to be consistent with the yields expected from examining the  $Q$ -values for reactions on light, target contaminants, specifically  $^{16}\text{O}$  and  $^{12}\text{C}$ . In particular, the peak in the yields for  $\Delta Z = -6$  from reactions on  $^{12}\text{C}$ , despite the smaller quantity of carbon backing, indicates that the positive  $Q$ -value has a dominant role. This is further supported by the observation in the EUROBALL-only data of fusion-evaporation products from a target with  $A \sim 14$ .

The BRS enabled both fusion-evaporation reaction products and binary reaction products to be studied in the same experiment. The ability to efficiently provide an accurate Doppler-shift correction for  $\gamma$ -ray events will form an important aspect at future radioactive beam facilities such as Spiral2 [25] and Fair [26]

## Acknowledgements

The authors would like to thank the Vivitron accelerator staff for the sulphur beam. Clausi Beschorner is thanked for their numerous contributions to the graphical sorting software. G. Duchêne, F. Haas and D.G. Jenkins are thanked for their contribution to part of the data collection. C.W. is grateful for the support of the Alexander von Humboldt Foundation. Tz.K. acknowledges a DAAD scholarship.

## References

- [1] W.N. Catford, C.N. Timis, R.C. Lemmon, M. Labiche, N.A. Orr, L. Caballero, R. Chapman, M. Freer, M. Chartier, H. Savajols, M. Rejmund, N. Amzal, N.I. Ashwood, T.D. Baldwin, M. Burns, N. Curtis, G. de France, W. Gelletly, X. Liang, S.D. Pain, V.P.E. Pucknell, B. Rubio, O. Sorlin, K. Spohr, Ch. Thiesen and D.D. Warner, *J.Phys.* **G31** (2005) S1655.

- [2] D.C. Radford, C. Baktash, C.J. Barton, J. Batchelder, J.R. Beene, C.R. Bingham, M.A. Caprio, M. Danchev, B. Fuentes, A. Galindo-Uribarri, J. Gomez del Campo, C.J. Gross, M.L. Halbert, D.J. Hartley, P. Hausladen, J.K. Hwang, W. Krolas, Y. Larochelle, J.F. Liang, P.E. Mueller, E. Padilla, J. Pavan, A. Piechaczek, D. Shapira, D.W. Stracener, R.L. Varner, A. Woehr, C.-H. Yua and N.V. Zamfir, Nucl. Phys **A752** (2005) 264c.
- [3] J.S. Winfield, W.N. Catford and N.A. Orr, Nucl. Instrum. and Meth. in Phys. Res. **A396** (1997) 147.
- [4] Peter Egelhof, Pramana **53** (1999) 365.
- [5] V. Zhrebchevsky, W. von Oertzen, D. Kamanin, B. Gebauer, S. Thummerer, Ch. Schulz and G. Royer, Phys. Lett. **B646** (2007) 12 and V. Zhrebchevsky, W. von Oertzen and D.V. Kamanin, JETP Lett. **85** (3) (2007) 136.
- [6] W. von Oertzen *et al.*, submitted to Phys. Rev. C.
- [7] W. von Oertzen *et al.*, to be submitted to Eur. Phys. J. A.
- [8] B. Gebauer *et al.*, in Proc. Int. Conf. on the future of nuclear spectroscopy, Crete, Greece (1993), eds. W. Gelletly *et al.*, p.168.
- [9] B. Gebauer *et al.*, Achievements with the Euroball spectrometer (2003) eds. W. Korten and S. Lunardi, p.135.
- [10] F. Ajzenberg-Selove, Nucl. Phys. **A506** (1990) 1.
- [11] D.C. Radford, Nucl. Instrum. and Meth. in Phys. Res. **A361** (1995) 297.
- [12] H.J. Wollersheim, D.E. Appelbe, A. Banu, R. Bassini, T. Beck, F. Becker, P. Bednarczyk, K.-H. Behr, M.A. Bentley, G. Benzoni, C. Boiano, U. Bonnes, A. Bracco, S. Brambilla, A. Brünle, A. Bürger, K. Burkard, P.A. Butler, F. Camera, D. Curien, J. Devin, P. Doornenbal, C. Fahlander, K. Fayz, H. Geissel, J. Gerl, M. Górska, H. Grawe, J. Grębosz, R. Griffiths, G. Hammond, M. Hellström, J. Hoffmann, H. Hübel, J. Jolie, J.V. Kalben, M. Kmiecik, I. Kojouharov, R. Kulesa, N. Kurz, I. Lazarus, J. Li, J. Leske, R. Lozeva, A. Maj, S. Mandal, W. Męczyński, B. Million, G. Münzenberg, S. Muralithar, M. Mutterer, P.J. Nolan, G. Neyens, J. Nyberg, W. Prokopowicz, V.F.E. Pucknell, P. Reiter, D. Rudolph, N. Saito, T.R. Saito, D. Seddon, H. Schaffner, J. Simpson, K.-H. Speidel, J. Styczeń, K. Sümmerer, N. Warr, H. Weick, C. Wheldon, O. Wieland, M. Winkler and M. Ziębliński, Nucl. Instr. Meth. **A537** (2005) 637.
- [13] B. Gebauer *et al.*, Nucl. Instrum. and Meth. in Phys. Res. A, to be published.
- [14] Ch. Schulz, Diploma Thesis, Hahn-Meitner-Institut and Technische Universität, Berlin (1995).
- [15] S. Thummerer, B. Gebauer, W. von Oertzen and M. Wilpert Il Nuovo Cimento, **A111**, 8-9 (1998) 1077.

- [16] S. Thummerer, Ph.D Thesis, Hahn-Meitner-Institut and Freie Universität, Berlin (1999) (URL: <http://www.diss.fu-berlin.de/2000/14/indexe.html>).
- [17] S. Thummerer, B. Gebauer, H.G. Bohlen, W. von Oertzen, D. Bazzacco, S.M. Lenzi, A. Algora, G. de Angelis, A. Gadea, D.R. Napoli, C. Borcan, F. Dönau, L. Käubler, H. Schnare, R. Schwengner, I. Peter, C. Beck, C. Bhattacharya, M. Rousseau, R. Nouicer and J. Lisle, *Phy. Scr.* **T88** (2000) 114.
- [18] *DATA8M graphical sorting software*, Martin and Thomas Wilpert, Hahn-Meitner-Institut (1996) unpublished. Extensively updated by Clausi Beschorner and Severin Thummerer, Hahn-Meitner-Institut (URL: <http://www.hmi.de/people/beschorner/data8m/html/data8m.html>).
- [19] C.R. Gould, D.R. Tilley and N.R. Roberson, *Phys. Rev.* **C7** (1973) 1068 and references therein.
- [20] F. Jundt, E. Aslanides, A. Gallman and E.K. Warburton, *Phys. Rev.* **C4** (1971) 498.
- [21] R.M. Lieder, H. Jäger, A. Neskakis and T. Venkova, *Nucl. Instrum. and Meth. in Phys. Res.* **220** (1984) 363.
- [22] T. Matuse, C. Beck, R. Noucier and D. Mahboub, *Phys. Rev.* **C55** (1997) 1380.
- [23] S.J. Sanders, A. Szanto de Toledo and C. Beck, *Phys. Rep.* **311** (1999) 487.
- [24] I. Ragnarsson, S. Åberg and R.K. Sheline, *Phys. Scr.* **24** (1981) 215.
- [25] *SPIRAL2 at GANIL: A world leading ISOL facility at the dawn of the next decade*, S. Gales, *Prog. in Part. and Nucl. Phys.* **59** (2007) 22.
- [26] *The Rare-Isotope-Beam facility at FAIR*, H. Emling, *Eur. Phys. J. - Special Topics*, **150** (2007) 235.